Chemical Science

ROYAL SOCIETY OF CHEMISTRY

EDGE ARTICLE

View Article Online
View Journal | View Issue

Cite this: *Chem. Sci.*, 2022, **13**, 10327

All publication charges for this article have been paid for by the Royal Society of Chemistry

Received 17th May 2022
Accepted 5th August 2022

DOI: 10.1039/d2sc02768b

rsc.li/chemical-science

Coherent ring-current migration of Mg-phthalocyanine probed by time-resolved X-ray circular dichroism†

Shichao Sun, * Haiwang Yong, Feng Chen and Shaul Mukamel *

The coherent ring current of Mg-phthalocyanine created by a broad band UV-visible pump pulse shows variation with time, where the ring currents at the corner benzene rings, around the Mg cation and on the outer ring oscillate with different time periods and the current density migrates among these regions. The 7 pairs of E_u degenerate excited states populated upon photoexcitation, generate 21 distinct coherent ring currents. We further calculate the time-resolved X-ray circular dichroism (TRXCD) spectrum of the coherences contributing to the ring current obtained by an attosecond X-ray probe pulse resonant with the nitrogen K-edge. A frequency domain TRXCD signal obtained by a Fourier transform of the signal with respect to the pump-probe delay time clearly separates the currents induced by different state pairs.

Controlling and measuring attosecond movements of electrons in molecules are of fundamental importance for photoinduced chemical reactions. Ring current, a circular electron motion, can be induced in cyclic conjugated molecules by applying a static magnetic field,[1–10] by using circularly polarized light (CPL)[11] or by coupling the molecule to an optical chiral cavity.[12] Magnetic-field-induced ring currents are widely applied in nuclear magnetic resonance,[8,13–15] where a static field non-resonant with electronic excited states perturbs the ground state and creates a ground state ring current. The direction of the magnetic field induced current is determined by the direction of the applied magnetic field and the aromaticity of the molecule, where aromatic (antiaromatic) molecules produce diamagnetic (paramagnetic) ring currents.[1,2,16–19]

In this theoretical study, we focus on the CPL induced ring currents, which are receiving considerable attention.[11,20–34] The sense of the resulting ring current is determined by the circular polarization of the pulse. Furthermore, CPL can create ring currents in selected states by tuning the pulse frequency to specific electronic states. This offers an additional control over the ring current generation.

We consider a molecule with two excited states with perpendicular transition dipoles to the ground state. We denote the excited states $|E_x\rangle$ and $|E_y\rangle$, whose transition dipole $\langle g|\boldsymbol{\mu}|E_{x,y}\rangle$ are along the x and y direction respectively. If the bandwidth of the circularly polarized pulse with polarization $\boldsymbol{\varepsilon}_\pm = \frac{\boldsymbol{\varepsilon}_x \pm i\boldsymbol{\varepsilon}_y}{2}$ covers both states, the pulse will excite them with a phase difference of $\frac{\pi}{2}$, giving the electron oscillation in x and y direction a $\frac{\pi}{2}$ phase difference, thus driving the electrons to move in a circle.[11]

If this pair of excited states is degenerate, by a linear combination, we can create a pair of degenerate current-carrying eigenstates $|E_\pm\rangle = \frac{|E_x\rangle \pm i|E_y\rangle}{\sqrt{2}}$.[11,30] A circularly polarized $\boldsymbol{\varepsilon}_\pm$ light pulse increases the population of state $|E_\pm\rangle$ respectively. Thus, the ring current created by the pulse can be viewed as population ring current which remains time-independent after the pump pulse is over. If the excited state pair is non-degenerate, the ring current is proportional to their coherence and is denoted coherent ring current.[24,25,35] After the pulse is over, the population is stationary while the coherent ring current oscillates with a period inversely proportional to the energy difference between the coherent states.

Previous research on coherent ring currents had focused on a single pair of coherence, where the current of the entire molecule evolves with the same pace.[11,20–26,28–30] Here, we study the ring-current dynamics resulting from the superposition of multiple ring-current pairs created by a broad band circularly pump pulse. Due to the interplay of multiple coherences, we find that the evolution of ring current at different locations in the molecule show distinct feature. As the coherent current density evolves with time, we see the redistribution of current density between different regions of the molecule, which can be viewed as current migration. This behavior is analogous to the

Department of Chemistry and Department of Physics & Astronomy, University of California, Irvine, USA. E-mail: shichas2@uci.edu; smukamel@uci.edu

† Electronic supplementary information (ESI) available: Coherent ring-current dynamics of Mg-phthalocyanine probed by time-resolved circular dichroism. See https://doi.org/10.1039/d2sc02768b

light-induced charge migration and the following evolution of electrons.[36,37,54] Localized ring currents created at different regions within the molecule, create new possibilities for designing molecular device.[38]

We focus on phthalocyanine which has broad applications in *e.g.* dye-sensitized solar cells[39,40] and photosensitizers for cancer photodynamic therapy.[41] Its derivative Mg-phthalocyanine (MgPc) has a rigid structure (see Fig. 1), which remains stable during the electronic dynamics.[42,43] MgPc has a high density of states belonging to the E_u irreducible representation (Table S1†), which facilitates the coherent excitation of many excited states. The molecule has multiple rings, including a central ring and the four benzene rings in the corners, which makes it possible to observe the dynamics of both local and global ring currents. We use a broadband UV pump pulse with 2 eV bandwidth made possible by recently developed attosecond UV-visible pulses.[44] Upon excitation, 7 pairs of degenerate excited states are populated within the pulse bandwidth to create 21 coherence pairs. These coherent ring currents have different profiles, giving rise to distinct evolution of local and the global ring currents. We further show that these coherences can be observed in time-resolved X-ray circular dichroism (TRXCD) spectrum resonant to the nitrogen K-edge. Contributions from each ring-current pair can be clearly identified in the Fourier-transformed CD spectrum.

As illustrated in Fig. 1, a circularly polarized pump pulse $\mathscr{E}_{\text{left}}(t) = E_0[\mathbf{e}_x \cos(\Omega(t)) - \mathbf{e}_y \sin(\Omega(t))]\exp\left[-\frac{t^2}{2\tau_{\text{pu}}{}^2}\right]$ propagating along z perpendicular to the molecular x–y plane with an amplitude of 6.9934×10^9 V m^{-1}, central frequency $\Omega = 4.0$ eV and duration of $\tau_{\text{pu}} = 4.64$ fs is applied at 0 fs to generate a ring current. The pulse duration and amplitude are chosen to excite 91.5% of the ground state population to excited states (Fig. S2†), thus create a high excited state population in this multi-level system. The mechanism is similar to Rabi-flop of two-level system. The electronic wave function is obtained by numerically solving the time-dependent Schrödinger equation $i\frac{\partial|\psi(t)\rangle}{\partial t} = [H_{\text{mol}} - \boldsymbol{\mu}\cdot\mathscr{E}_{\text{left}}(t)]|\psi(t)\rangle$, where H_{mol} is the molecular Hamiltonian and the wave function is expanded in the molecular ground and valence excited states basis $|\psi(t)\rangle = \sum_{\text{A}} a_{\text{A}}(t)|\text{A}\rangle$. Atomic units are used throughout. MgPc belongs to the D_{4h} point group. Its excited states are obtained by a TDDFT calculation. The molecular geometry is optimized using DFT with the B3LYP functional[45–48] and the 6-31g(d) basis set and Gaussian 16.[49] Both valence and core excited states are computed with TDDFT in the Tamm–Dancoff approximation (TDA) using the Chronus Quantum software package.[50] The TDA calculations employ the same density functional and basis set used in the geometry optimization. The valence excited states are listed in Table S1.† For CPL with circularly polarization in x–y plane, the excited states of E_u irreducible representation with two-fold degeneracy are dipole allowed, and denoted mE_ux and mE_uy, where x, y denote the transition dipole direction, and m, $n = 1$, 2, …, 7 is the index of pair of degenerate states. The state with A_{2u} irreducible representation has transition dipole $\langle g|\boldsymbol{\mu}|e\rangle$ along z and is thus not excited by the pump pulse. The current density is given by[51]

$$\mathbf{j}(\mathbf{r},\mathbf{t}) = \sum_{\text{A,B}} D_{\text{BA}}(\mathbf{t})\mathbf{j}_{\text{AB}}(\mathbf{r}) \tag{1}$$

$$\mathbf{j}_{\text{AB}}(\mathbf{r}) = \sum_{\mu\nu} D^{\text{BA}}_{\nu\mu}\left(\chi^*_\mu(\mathbf{r})\nabla\chi_\nu(\mathbf{r}) - \nabla\chi^*_\mu(\mathbf{r})\chi_\nu(\mathbf{r})\right) \tag{2}$$

where A, B run over the ground and valence excited states, $D_{\text{BA}}(t) = a^*_{\text{A}}(t)a_{\text{B}}(t)$ is the density matrix at time t, $a_{\text{B}}(t)$ is the coefficient of electronic states. $D^{\text{BA}}_{\nu\mu}$ is the transition one-electron density matrix (1PDM) between electronic state B and A in the atomic orbital basis and νμ denote atomic orbital. $\chi_\mu(\mathbf{r})$ and $\nabla\chi_\mu(\mathbf{r})$ are the atomic orbital basis and its gradient respectively.

The induced ring current is further probed by the TRXCD signal at the nitrogen K-edge. The Gaussian X-ray probe pulse has central frequency $\omega_c = 383.172$ eV, $\sigma = 0.7$ fs and time delay T scanned from 0 to 25 fs. The TRXCD signal is derived in ESI S1† using time dependent perturbation theory in the probe pulse–molecule interaction

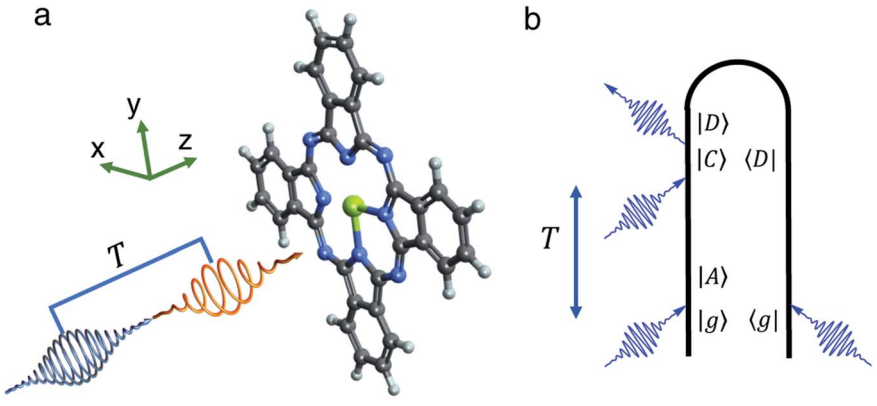

Fig. 1 (a) Sketch of the pump probe experiment. Mg-Pc is pumped by a circularly polarized UV-visible short pulse (orange arrow) and creates a coherent ring current. The coherence is detected by the TRXCD signal using an X-ray probe pulse (blue arrow) with a time delay T. (b) Loop diagram of X-ray TRXCD. Only the excited state absorption contribution is relevant to our study.

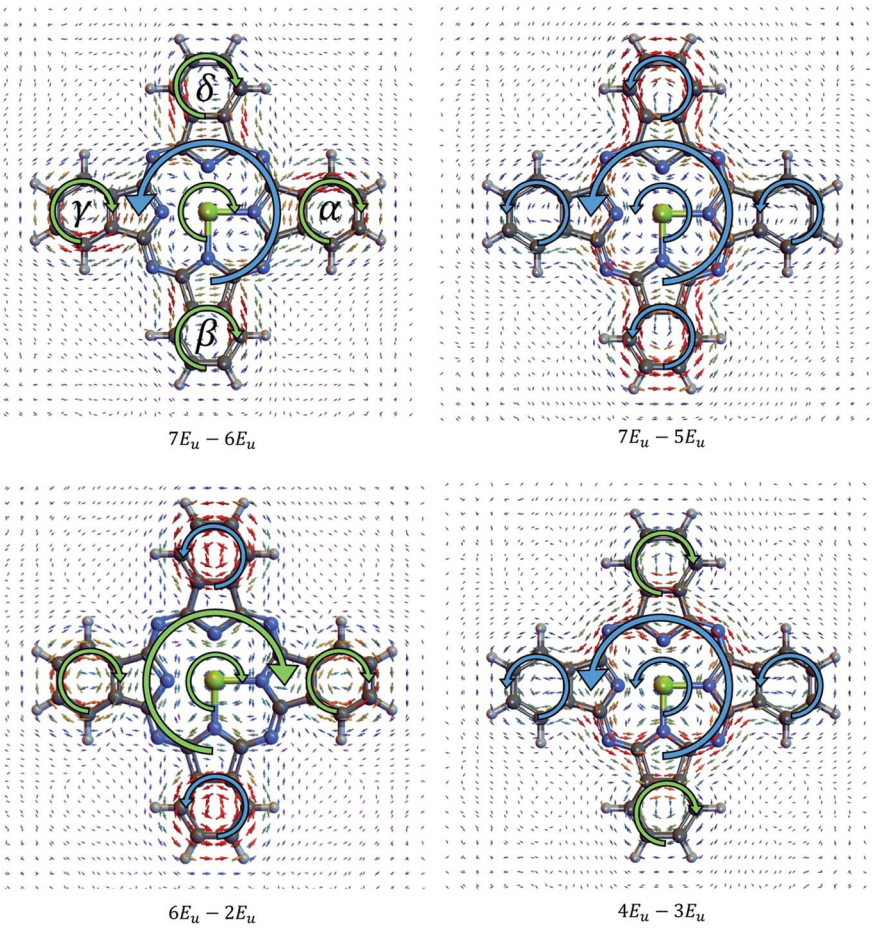

Fig. 2 Current density of the coherence between pair $7E_u$–$6E_u$, $7E_u$–$5E_u$, $6E_u$–$2E_u$, $4E_u$–$3E_u$ respectively. Counter-clockwise local current directions are marked with big thick blue arrows while clockwise local current directions are marked with thick light green arrows.

$$S_{\mathrm{TRXCD}}(\omega, T) = 2\sqrt{2\pi}\sigma\ \mathrm{Re}\left\{ \sum_{\mathrm{A,D=g,val C=core}} \sum \frac{\mathbf{j}_{\mathrm{DC}}(\mathbf{k}) \times \mathbf{j}^{\dagger}_{\mathrm{CA}}(-\mathbf{k})}{\omega_{\mathrm{DC}} + \omega + i\Gamma} \cdot \boldsymbol{\varepsilon}_{\kappa} \int_0^{+\infty} \mathrm{d}t\ \mathrm{e}^{i(\omega-\omega_{\mathrm{c}})(t-T)}\ \mathrm{e}^{-\frac{1}{2}\left[\frac{(t-T)^2}{\sigma^2}+\sigma^2(\omega-\omega_{\mathrm{c}})^2\right]} a^{*}_{\mathrm{D}}(t) a_{\mathrm{A}}(t) \right\} \quad (3)$$

where A, D run over the ground and valence excited states and C denotes core excited states. We employed the minimal coupling Hamiltonian for calculating the CD signal, where the transition current density is used in the CD expression instead of multipole moments.[51,52] The minimal coupling expression includes implicitly the contributions to all orders of multipolar moments.[51,52] Since CPL induces ring current only for oriented molecule,[20] the TRXCD signal is simulated for oriented molecules. $\boldsymbol{\varepsilon}_{\kappa}$ is the propagation unit vector of the probe pulse, and $\mathbf{k} = \frac{\omega}{c}\boldsymbol{\varepsilon}_{\kappa}$. $\mathbf{j}_{\mathrm{DC}} = \int \mathrm{d}\mathbf{r}\, \mathbf{j}_{\mathrm{DC}}(\mathbf{r})\mathrm{e}^{-i\mathbf{k}\cdot\mathbf{r}}$ is the momentum space transition current density. ω_{DC} is the transition energy from state C to D. ω is the angular frequency. $\Gamma = 0.093$ eV is core line width for nitrogen.[53] Here we focus on the nitrogen K-edge since the Mg line width ($\Gamma = 0.45$ eV)[53] is too broad to resolve different excited states as shown in Fig. S2.†

Ring current migration and the corresponding excited state coherences

The ring-currents formed by a pair of degenerate states populations, for example the mE_u reach a stationary value after the pulse is over. Ring-currents can also be formed by the coherence between states which belong to different degenerate pairs, for example, the coherence $mE_u x$–$nE_u y$, where $m \neq n$. This coherence oscillates in time with the period $\frac{2\pi}{|\omega_{mE_u, nE_u}|}$.

During the pulse, the ground/excited state (g–ex) coherence makes a large contribution to the current. When the pulse is switched off, the coefficient of ground state is small, thus the fast oscillatory component of induced ring current becomes weaker as shown in Fig. S4.† Since the oscillation is faster than the probe pulse duration, the g–ex coherence is not resolved by the TRXCD signal. We thus focus on the excited state-excited state (ex–ex) coherences, which contribute to slower components of the ring current.

The ring currents associated with different ex–ex coherence pairs $\mathbf{j}_{AB}$ have distinct spatial profiles. Ring currents can arise in four zones in the MgPc molecule. First is in the center around Mg cation denoted "CT", second is the current on the outer ring denoted "OT", third is the current on the right and left benzene rings denoted "α" and "γ" respectively, fourth is the lower and upper benzene rings labelled "β" and "δ" respectively, as shown in Fig. 2. Currents associated with several pairs of states are shown in Fig. 2. For the same coherence, the ring current at different locations can have a different direction. For example, the $7E_u$–$5E_u$ coherent ring current has the same direction around the Mg (CT) and on the outer loop (OT), while for the $7E_u$–$6E_u$ current, the direction of CT and OT are opposite. The direction of the α, γ and β, δ ring currents are the same in $7E_u$–$5E_u$ and $7E_u$–$6E_u$, while in $6E_u$–$2E_u$ and $4E_u$–$3E_u$, the α, γ and β, δ have opposite direction.

As each component of the coherent ring current $\mathbf{j}_{mE_u,nE_u}$ oscillates with its own period of $\frac{2\pi}{|\omega_{mE_u,nE_u}|}$, the total induced ring current varies with time, where the current evolutions at different locations is unsynchronized. This behavior is different from the ring current induced by narrow band pump,[35] where the ring current in the entire molecule oscillates uniformly.

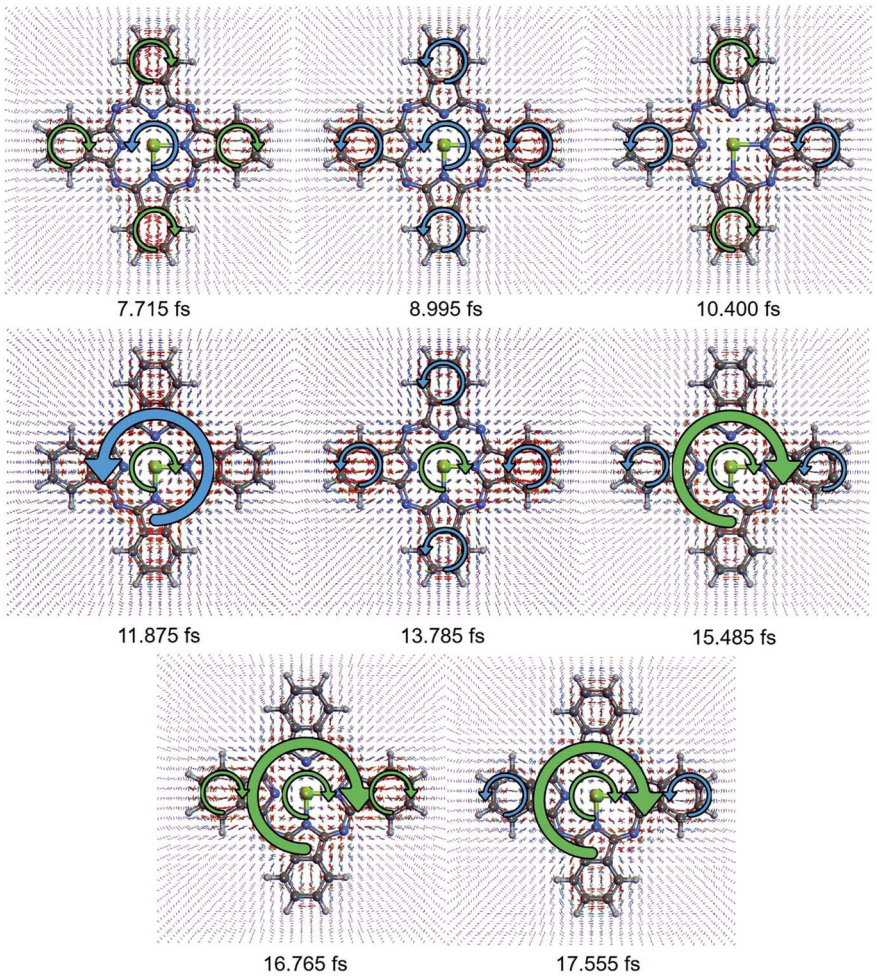

Fig. 3 Snapshots of the total ex–ex ring current at different times after the pump. The ring current direction is marked by a green arrow (clockwise) and blue arrow (counter-clockwise) respectively. From 7.715 fs to 8.995 fs, the current on the outer four benzene rings change from clockwise to counter-clockwise while the current around Mg atom (CT) is unchanged. From 8.995 fs to 10.400 fs, the ring currents on the upper and lower corner rings (β, δ) change to clockwise, while the CT ring current disappear. Then at 11.875 fs, the ring currents around four small corner rings disappear, while the counter-clockwise outer ring current (OT) and clockwise CT ring current appears. Then at 13.785 fs, the counter-clockwise ring current around four corner rings appear, while the OT ring current disappear, and the clockwise CT ring current remain intact. At 15.485 fs, the clockwise OT ring current is formed while the counter-clockwise current in the β, δ ring disappear. At 16.765 fs, the current at left and right corner ring change from counter-clockwise to clockwise, and then change back to counter-clockwise at 17.555 fs.

This unsynchronized evolution of currents at different zones causes the redistribution of current density, resulting in the current migration in the whole molecule. The total ex–ex coherent ring current profile at various time delays T after CPL are depicted in Fig. 3. We show the local ring current profiles at the four corner benzene rings (α, γ and β, δ), the center zone around Mg (CT), and the outer loop of the total molecule (OT) reverse direction at different times. For example, at 7.715 fs, α, γ and β, δ are clockwise whereas CT is counter-clockwise. At 8.995 fs, all currents are counter-clockwise. Between 7.715 fs and 8.995 fs, α, γ and β, δ change from clockwise to counter-clockwise while CT is unchanged. From 8.995 fs to 10.400 fs, the β, δ change to clockwise, while CT vanishes. Moving to 11.875 fs, the ring current around α, γ and β, δ disappear, while a counter-clockwise OT ring current and clockwise ring current CT appear. Then at 13.785 fs, counter-clockwise currents α, γ and β, δ rings appear, the OT ring current disappears, and the clockwise ring current CT remains intact. At 15.485 fs, the clockwise current OT is formed while the counter-clockwise current in the β, δ current vanishes. At 16.765 fs, the current α, γ changes from counter-clockwise to clockwise, and then changes back to counter-clockwise at 17.555 fs.

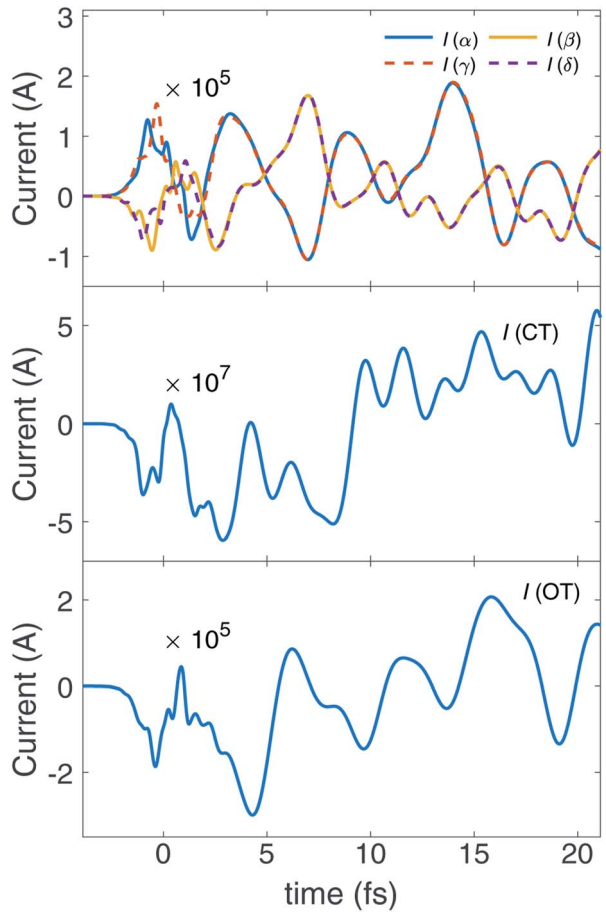

Fig. 4 Time evolution of local ring current induced by excited state-excited state coherence. From top to bottom, the plots are ring currents of the four corner benzene rings (α, β, γ and δ ring), around the Mg atom at center (CT) and the outer ring (OT). Currents in Ampere are calculated by numerically integrating the current density at a plane, as illustrated in Fig. S8.† Positive values of currents indicate clockwise ring current. After the pump pulse, the currents of γ/δ are identical to α/β. We can clearly see the currents migrate between ring αγ and βδ.

The time evolution of the local ring currents is plotted in Fig. 4. The currents in ampere are calculated by integrating the current density on a plane. Details of the integration are explained in ESI S9.† After the pump pulse, the corner rings at opposite position (like α, γ and β, δ) have the same ring current rotation direction, while neighboring rings have no such relationship. This is due to the fact that these coherent ring currents are generated by excited states with E_u irreducible representation whose $\mathbf{j}_{mE_u,nE_u}$ are invariant under C_2 rotation with respect to the principle axis. We can clearly see the transfer of ring currents among the four corner rings, between {α, γ} and {β, δ}. Overall, Fig. 4 depicts the unsynchronized evolution of the current at four different zones (CT, OT, α, γ and β, δ). The redistribution of ring currents among these zones results in ring current migration dynamics.

In summary, the coherent ring current induced by a broad band pump pulse for a multi-ring molecule can change its direction and magnitude locally, in contrast to changing the total ring current direction globally when a narrow band pulse is applied. The ring current migration among different zones in the molecule is caused by the interplay of multiple pairs of coherent ring currents. The directions and strengths of induced ring current result in an induced magnetic field, computed with Biot–Savart law, as displayed in Fig. S4 and S5.† The induced magnetic field is further decomposed into the contributions of different coherences.

The time-resolved circular dichroism signal at the K-edge

For the time domain TRXCD signal $S(\omega,T)$ in the upper panel of Fig. 5, peaks are located where ω coincides with valence to a core excitation energy ω_{CD}. The peak intensity is proportional to the numerator $\mathbf{j}_{DC} \times \mathbf{j}^{\dagger}_{CA}$ of eqn (3) and the coherence $a^{*}_{D}a_{A}$. To assign each peak to a valence-core excitation, we take a vertical slice of the spectrum at time 10.40 fs from the TRXCD and identify important valence to core state transitions as described in ESI.†

The time dependence of the TRXCD signal arises from the coherence between E_u states. To separate the signals with different oscillation period, we perform a Fourier transform of the time domain TRXCD signal $S(\omega,T)$ with respect to the delay time T which results in the frequency domain signal $\tilde{S}(\omega,\omega')$. Since the pump pulse is centered at 0 fs, the pump pulse driven part of the TRXCD spectrum is eliminated by taking the Fourier transform for the TRXCD in the 3.72 fs to 21.10 fs interval. The Fourier transformed CD spectra as a function of the oscillation frequency ω' and excitation energy $\hbar\omega$ is depicted in the lower panel of Fig. 5. The $\hbar\omega'$ value of the bright colored peaks indicates the energy difference of the coherent states, which coincides with oscillation angular frequency of the coherence. Table 1 lists the coherences as well as their oscillation frequencies.

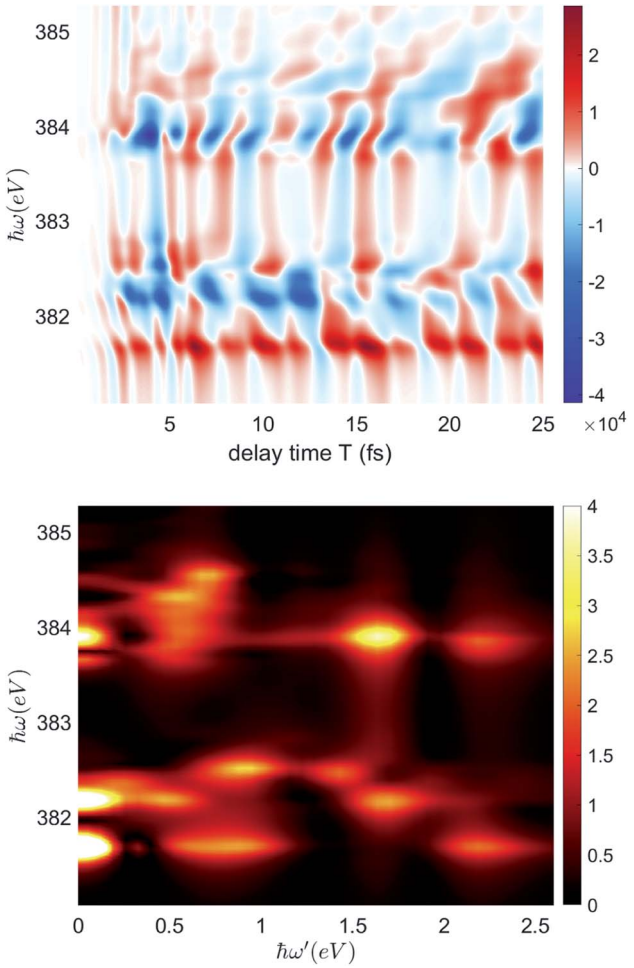

Fig. 5 Upper panel: Simulated nitrogen K-edge X-ray TRXCD signal eqn (3). The delay time T is scanned from 0 fs to 25 fs. The intensity of the signal is in arbitrary units. Lower panel: Fourier transformed circular dichroism spectrum of nitrogen K-edge. $\hbar\omega$ is detection frequency and $\hbar\omega'$ is the conjugate variable of delay time T. For each bright peak, the $\hbar\omega$ is the excitation energy and the $\hbar\omega'$ values indicate the frequency of oscillation corresponding to the coherence contributing to the peak.

The CD signal at peak energies and the corresponding coherence frequencies

We first consider the peaks for $\hbar\omega' = 0$ in the lower panel of Fig. 5, which originate from the time independent population ring current. The peaks at $\hbar\omega = 381.6788$, 383.669, 383.8017 eV represent the population ring current of $7E_u$, with excitation to core states 7, 23, 25 respectively (see ESI S2† for the labels of core excited states).

The remaining peaks correspond to coherent ring currents. $\hbar\omega'$ indicates the energy gap between the coherent states, resolved in Fig. 5, with both energy gaps of the coherent states and the coherence frequency obtained from the peaks listed in Table 1. The coherence pairs with a similar energy gap can be separated by different core state excitation energy $\hbar\omega$, for example, $4E_u$–$1E_u$ and $5E_u$–$1E_u$. Such separation can be achieved for the nitrogen K-edge but not in the Mg K-edge due to its large line width.[53] With the aid of ω and ω', each peak in Fig. 5 assigned to a coherence with its valence to core transitions is listed in Table 1.

The coherence with longest period is $4E_u$–$3E_u$ with an energy difference of 0.1023 eV. It contributes to the peak at $\hbar\omega = 382.4157$ eV with coherence frequency $\hbar\omega' = 0.2377$ eV. Since the total simulation time is kept short to avoid decoherence, the $4E_u$–$3E_u$ coherence did not complete a single period, which causes the deviation of ω' from the energy difference.

The brightest peak at $\hbar\omega' = 1.6374$ eV and $\hbar\omega = 383.9051$ eV corresponds to the excitation from $1E_u$ to core state 7, contributed by $5E_u$–$1E_u$ coherence.

At $\hbar\omega' = 0.5354$ eV, the peaks with excitation energy between 383.6 and 384.5 eV correspond to the transition from $7E_u$ and $5E_u$ to different core excited states, contributed by the $7E_u$–$5E_u$ coherence. The peaks at $\hbar\omega = 384.2041$, 384.3369 eV represent the excitation from $5E_u$ to core state 22 and 25 respectively; peak at 383.669 eV and 383.8017 are excitation from $7E_u$ to core state 22 and state 25 respectively.

Decoherence effects

The ring current is expected to decay due to the interaction of electronic system with a nuclear bath. Such dephasing effects are not included in the Schrödinger equation, but can be described phenomenologically. Pure dephasing can be included by (1) multiplying the signal expression eqn (3) by a dephasing factor $e^{-\Gamma_{1,DA}\tau}$, where $\Gamma_{1,DA}$ is the valence–valence coherence dephasing rate and (2) add a term $i\Gamma_{2,DC}$ to the denominator of eqn (3) as given in the ESI.† In Section S8,† the TRXCD spectra and the Fourier transformation are shown for different values of dephasing rates, *i.e.*, from 1/100 fs^{-1} to 1/10 fs^{-1} (Fig. S7†). The valence states-core states dephasing broadens the peak in energy domain $\hbar\omega$. Since the dephasing rate contribution is less than the lifetime broadening of core excited states, this effect is not significant. The valence excited state-valence excited state dephasing causes a decay of the TRXCD signal with the delay time T. Higher dephasing rates result in earlier decay of TRXCD signal in time domain, as well as lower resolution in frequency domain $\hbar\omega'$. Nevertheless, distinct coherence components can still be assigned in the Fourier transformed spectrum even with a high dephasing rate of 1/10 fs^{-1}. The dephasing of ground state–valence excited state does not affect the TRXCD signal, since such coherence has shorter oscillation period than the probe pulse duration, thus not observed in the signal. In summary, although dephasing of coherence results in lower resolution of the spectra, it does not change peak assignments.

Apart from dephasing, the coherence of excited states can cause magnetic dipole radiation, since the transition magnetic dipoles between excited state of E_u irreducible representation are nonzero while their transition electric dipoles vanish. This radiation causes damping of excited states. However, since the magnetic dipole radiation is weak, this effect is ignored in our simulation.

In conclusion, a broad band (2 eV) UV-visible circularly polarized pump pulse is used in this study to create a superposition of 7 degenerate pairs of excited states. The coherent ring

Table 1 The coherence contributing to the TRXCD spectrum including the energy difference of the coherent states as well as coherence frequency $\hbar\omega'$ obtained from the x-axis value of the bright peaks in Fig. 5

Coherence	Period (fs)	Energy difference (eV)	Coherence frequency $\hbar\omega'$ (eV)	Excitation energy $\hbar\omega$ (eV)	Transition valence to core
$4E_u$–$3E_u$	40.427	0.1023	0.2377	382.4157	$4E_u$ to core states 6
$7E_u$–$6E_u$	8.545	0.4840	0.4666	382.1627	$6E_u$ to core state 7, 8
$7E_u$–$5E_u$	7.726	0.5353	0.5354	384.2041	$5E_u$ to core state 22
				384.3369	$5E_u$ to core state 25
				383.6690	$7E_u$ to core state 22
				383.8017	$7E_u$ to core state 25
$7E_u$–$3E_u$	4.929	0.8391	0.8798	381.6788	$7E_u$ to core state 7, 8
				382.5179	$3E_u$ to core state 6
$4E_u$–$1E_u$	2.776	1.4896	1.4308	382.4157	$4E_u$ to core states 6
$5E_u$–$1E_u$	2.446	1.6911	1.6374	383.9051	$1E_u$ to core state 7
$6E_u$–$1E_u$	2.374	1.7424	1.7063	381.6788	$7E_u$ to core state 7, 8
				382.1627	$6E_u$ to core state 7, 8
$7E_u$–$1E_u$	1.858	2.2264	2.1884	383.9051	$1E_u$ to core state 7

currents at different locations in the molecule show distinct features, where the coherent ring current on the corner rings, outer ring and inner ring around the Mg evolve unsynchronizedly due to the interplay of many coherence pairs of Mg-Pc excited states. This coherence may be probed by time-resolved X-ray circular dichroism spectrum at the nitrogen K-edge. By Fourier transforming the CD signal with respect to the probe delay time T, we obtain the CD spectrum as a function of excitation energy and oscillation frequency. Bright peaks are assigned to pairs of excited state coherence by the coherence frequency and its excitation energy in the two dimensional spectrum Fig. 5. This suggests a way to probe the evolution of ring current in time domain and separate individual excited state coherence contributing to the coherent ring current in the frequency domain. The redistribution of current density within the molecule pave the way for controlling the local electron movement within the molecule, enabling light control of electron at sub-molecular scale and femtosecond time scale.

Data availability

All study data are included in the article and/or ESI.†

Author contributions

S. M. supervised and conceived the project. S. S. and F. C. derived the equations for the signal. S. S. performed the electronic structure calculations. S. S., F. C. and H. Y. performed spectroscopy simulations. All authors contributed to the analysis and interpretation of the results, and wrote the manuscript.

Conflicts of interest

There are no conflicts to declare.

Acknowledgements

The support of the National Science Foundation through Grant No. CHE-1953045 is gratefully acknowledged. S. M. was supported by the U.S. Department of Energy, Office of Science, Office of Basic Energy Sciences under Award DE-FG02-04ER15571. S. M. is a fellow of the Hagler Institute for Advanced Study at Texas A&M University.

References

1 F. London, Théorie quantique des courants interatomiques dans les combinaisons aromatiques, *J. Phys. Radium*, 1937, **8**, 397–409.
2 R. Breslow, Antiaromaticity, *Acc. Chem. Res.*, 1973, **6**, 393–398.
3 P. Lazzeretti, Ring Currents, *Prog. Nucl. Magn. Reson. Spectrosc.*, 2000, **36**, 1–88.
4 J. Jusélius and D. Sundholm, The Aromatic Character of Magnesium Porphyrins, *J. Org. Chem.*, 2000, **65**, 5233–5237.
5 E. Steiner and P. W. Fowler, Patterns of Ring Currents in Conjugated Molecules: A Few-Electron Model Based on Orbital Contributions, *J. Phys. Chem. A*, 2001, **105**, 9553–9562.
6 G. Merino, T. Heine and G. Seifert, The Induced Magnetic Field in Cyclic Molecules, *Chem.–Eur. J.*, 2004, **10**, 4367–4371.
7 E. Steiner, A. Soncini and P. W. Fowler, Ring Currents in the Porphyrins: π Shielding, Delocalisation Pathways and the Central Cation, *Org. Biomol. Chem.*, 2005, **3**, 4053–4059.
8 T. Heine, C. Corminboeuf and G. Seifert, The Magnetic Shielding Function of Molecules and Pi-Electron Delocalization, *Chem. Rev.*, 2005, **105**, 3889–3910.
9 B. Kudisch, M. Maiuri, L. Moretti, M. B. Oviedo, L. Wang, D. G. Oblinsky, R. K. Prud'homme, B. M. Wong, S. A. McGill and G. D. Scholes, Ring Currents Modulate Optoelectronic Properties of Aromatic Chromophores at 25 T, *Proc. Natl. Acad. Sci. U. S. A.*, 2020, **117**, 11289–11298.
10 M. D. Peeks, T. D. Claridge and H. L. Anderson, Aromatic and Antiaromatic Ring Currents in a Molecular Nanoring, *Nature*, 2017, **541**, 200–203.
11 I. Barth, J. Manz, Y. Shigeta and K. Yagi, Unidirectional Electronic Ring Current Driven by a Few Cycle Circularly Polarized Laser Pulse: Quantum Model Simulations for

Mg- porphyrin, *J. Am. Chem. Soc.*, 2006, **128**, 7043–7049, PMID: 16719485.
12 S. Sun, B. Gu and S. Mukamel, Polariton Ring Currents and Circular Dichroism of Mg-porphyrin in a Chiral Cavity, *Chem. Sci.*, 2022, **13**, 1037–1048.
13 L. Jackman, F. Sondheimer, Y. Amiel, D. Ben-Efraim, Y. Gaoni, R. Wolovsky and A. Bothner-By, The Nuclear Magnetic Resonance Spectroscopy of a Series of Annulenes and Dehydro-Annulenes, *J. Am. Chem. Soc.*, 1962, **84**, 4307–4312.
14 R. H. Mitchell, Measuring Aromaticity by NMR, *Chem. Rev.*, 2001, **101**, 1301–1316, PMID: 11710222.
15 A. D. Allen and T. T. Tidwell, Antiaromaticity in Open-Shell Cyclopropenyl to Cycloheptatrienyl Cations, Anions, Free Radicals, and Radical Ions, *Chem. Rev.*, 2001, **101**, 1333–1348.
16 L. Pauling, The Diamagnetic Anisotropy of Aromatic Molecules, *J. Chem. Phys.*, 1936, **4**, 673–677.
17 J. Pople, Proton Magnetic Resonance of Hydrocarbons, *J. Chem. Phys.*, 1956, **24**, 1111.
18 J. Pople and K. Untch, Induced Paramagnetic Ring Currents, *J. Am. Chem. Soc.*, 1966, **88**, 4811–4815.
19 J. Gomes and R. Mallion, Aromaticity and Ring Currents, *Chem. Rev.*, 2001, **101**, 1349–1384.
20 I. Barth and J. Manz, Periodic Electron Circulation Induced by Circularly Polarized Laser Pulses: Quantum Model Simulations for Mg Porphyrin, *Angew. Chem., Int. Ed.*, 2006, **45**, 2962–2965.
21 I. Barth and J. Manz, Electric Ring Currents in Atomic Orbitals and Magnetic Fields Induced by Short Intense Circularly Polarized π Laser Pulses, *Phys. Rev. A: At., Mol., Opt. Phys.*, 2007, **75**, 012510.
22 I. Barth, J. Manz and L. Serrano-Andrés, Quantum Simulations of Toroidal Electric Ring Currents and Magnetic Fields in Linear Molecules Induced by Circularly Polarized Laser Pulses, *Chem. Phys.*, 2008, **347**, 263–271, Ultrafast Photoinduced Processes in Polyatomic Molecules.
23 M. Kanno, H. Kono, Y. Fujimura and S. H. Lin, Nonadiabatic Response Model of Laser-Induced Ultrafast π-Electron Rotations in Chiral Aromatic Molecules, *Phys. Rev. Lett.*, 2010, **104**, 108302.
24 H. Mineo, M. Yamaki, Y. Teranishi, M. Hayashi, S. H. Lin and Y. Fujimura, Quantum Switching of π-Electron Rotations in a Nonplanar Chiral Molecule by Using Linearly Polarized UV Laser Pulses, *J. Am. Chem. Soc.*, 2012, **134**, 14279–14282.
25 M. Kanno, Y. Ono, H. Kono and Y. Fujimura, Laser-Polarization Effects on Coherent Vibronic Excitation of Molecules with Quasi-Degenerate Electronic States, *J. Phys. Chem. A*, 2012, **116**, 11260–11272, PMID: 22834970.
26 H. Mineo, S. Lin and Y. Fujimura, Coherent π-Electron Dynamics of (P)-2,2′-biphenol Induced by Ultrashort Linearly Polarized UV Pulses: Angular Momentum and Ring Current, *J. Chem. Phys.*, 2013, **138**, 074304.
27 H. Mineo, S. Lin and Y. Fujimura, Vibrational Effects on UV/Vis Laser-Driven π-Electron Ring Currents in Aromatic Ring Molecules, *Chem. Phys.*, 2014, **442**, 103–110.
28 J. J. Rodriguez and S. Mukamel, Probing Ring Currents in Mg-Porphyrins by Pump–Probe Spectroscopy, *J. Phys. Chem. A*, 2012, **116**, 11095–11100, PMID: 22881200.
29 K.-J. Yuan, C.-C. Shu, D. Dong and A. D. Bandrauk, Attosecond Dynamics of Molecular Electronic Ring Currents, *J. Phys. Chem. Lett.*, 2017, **8**, 2229–2235, PMID: 28468499.
30 M. Kanno, H. Kono and Y. Fujimura, Laser-Control of Ultrafast π-Electron Ring Currents in Aromatic Molecules: Roles of Molecular Symmetry and Light Polarization, *Appl. Sci.*, 2018, **8**, 2347.
31 K. R. Nandipati and O. Vendrell, On the Generation of Electronic Ring Currents under Vibronic Coupling Effects, *J. Chem. Phys.*, 2020, **153**, 224308.
32 K. R. Nandipati and O. Vendrell, Dynamical Jahn-Teller effects on the generation of electronic ring currents by circularly polarized light, *Phys. Rev. Res.*, 2021, **3**, L042003.
33 S. Eckart, *et al.*, Ultrafast Preparation and Detection of Ring Currents in Single Atoms, *Nat. Phys.*, 2018, **14**, 701–704.
34 O. Neufeld and O. Cohen, Background-Free Measurement of Ring Currents by Symmetry-Breaking High-Harmonic Spectroscopy, *Phys. Rev. Lett.*, 2019, **123**, 103202.
35 Y. Nam, J. R. Rouxel, J. Y. Lee and S. Mukamel, Monitoring Aromatic Ring-Currents in Mg-Porphyrin by Time-Resolved Circular Dichroism, *Phys. Chem. Chem. Phys.*, 2020, **22**, 26605–26613.
36 H. J. Wörner, C. A. Arrell, N. Banerji, A. Cannizzo, M. Chergui, A. K. Das, P. Hamm, U. Keller, P. M. Kraus, E. Liberatore, *et al.*, Charge migration and charge transfer in molecular systems, *Struct. Dyn.*, 2017, **4**, 061508.
37 L. S. Cederbaum and J. Zobeley, Ultrafast charge migration by electron correlation, *Chem. Phys. Lett.*, 1999, **307**, 205–210.
38 M. Di Ventra, S. Pantelides and N. Lang, First-principles calculation of transport properties of a molecular device, *Phys. Rev. Lett.*, 2000, **84**, 979.
39 M. G. Walter, A. B. Rudine and C. C. Wamser, Porphyrins and Phthalocyanines in Solar Photovoltaic Cells, *J. Porphyrins Phthalocyanines*, 2010, **14**, 759–792.
40 M. Urbani, M.-E. Ragoussi, M. K. Nazeeruddin and T. Torres, Phthalocyanines for Dye-Sensitized Solar Cells, *Coord. Chem. Rev.*, 2019, **381**, 1–64.
41 Z. Jiang, J. Shao, T. Yang, J. Wang and L. Jia, Pharmaceutical development, composition and quantitative analysis of phthalocyanine as the photosensitizer for cancer photodynamic therapy, *J. Pharm. Biomed. Anal.*, 2014, **87**, 98–104.
42 J. Mi, L. Guo, Y. Liu, W. Liu, G. You and S. Qian, Excited-State Dynamics of Magnesium Phthalocyanine Thin Film, *Phys. Lett. A*, 2003, **310**, 486–492.
43 D. Potamianos, M. Nuber, A. Schletter, M. Schnitzenbaumer, M. Haimerl, P. Scigalla, M. Wörle, L. I. Wagner, R. Kienberger and H. Iglev, Full Dynamics Description of Mg Phthalocyanine Crystalline and Amorphous Semiconductor Systems, *J. Phys. Chem. C*, 2021, **125**, 18279–18286.
44 M. T. Hassan, T. T. Luu, A. Moulet, O. Raskazovskaya, P. Zhokhov, M. Garg, N. Karpowicz, A. Zheltikov, V. Pervak,

F. Krausz and E. Goulielmakis, Optical Attosecond Pulses and Tracking the Nonlinear Response of Bound Electrons, *Nature*, 2016, **530**, 66–70.

45 A. D. Becke, Density-Functional Exchange-Energy Approximation with Correct Asymptotic Behavior, *Phys. Rev. A: At., Mol., Opt. Phys.*, 1988, **38**, 3098.

46 A. D. Becke, Density-Functional Thermochemistry. III. The Role of Exact Exchange, *J. Chem. Phys.*, 1993, **98**, 5648.

47 C. Lee, W. Yang and R. G. Parr, Development of the Colle-Salvetti Correlation-Energy Formula into a Functional of the Electron Density, *Phys. Rev. B: Condens. Matter Mater. Phys.*, 1988, **37**, 785.

48 B. Miehlich, A. Savin, H. Stoll and H. Preuss, Results Obtained with the Correlation Energy Density Functionals of Becke and Lee, Yang and Parr, *Chem. Phys. Lett.*, 1989, **157**, 200–206.

49 M. J. Frisch, *et al.*, *Gaussian 16 Revision A.03*, Gaussian Inc., Wallingford CT, 2016.

50 D. B. Williams-Young, A. Petrone, S. Sun, T. F. Stetina, P. Lestrange, C. E. Hoyer, D. R. Nascimento, L. Koulias, A. Wildman, J. Kasper, J. J. Goings, F. Ding, A. E. DePrince III, E. F. Valeev and X. Li, The Chronus Quantum Software Package, *Wiley Interdiscip. Rev.: Comput. Mol. Sci.*, 2019, e1436.

51 J. R. Rouxel, M. Kowalewski and S. Mukamel, Current *vs.* Charge Density Contributions to Nonlinear X-ray Spectroscopy, *J. Chem. Theory Comput.*, 2016, **12**, 3959–3968.

52 J. R. Rouxel, V. Y. Chernyak and S. Mukamel, Non-local real-space analysis of chiral optical signals, *Chem. Sci.*, 2016, **7**, 6824–6831.

53 J. Campbell and T. Papp, Widths of the Atomic K–N7 Levels, *At. Data Nucl. Data Tables*, 2001, **77**, 1–56.

54 G Hermann, V Pohl, G Dixit and JC Tremblay, Probing Electronic Fluxes via Time-Resolved X-Ray Scattering, *Phys. Rev. Lett.*, 2020, **124**(1), 013002.